Volume 10
Number 11
21 March 2022
Pages 5653–6252

# Journal of Materials Chemistry A

Materials for energy and sustainability

rsc.li/materials-a

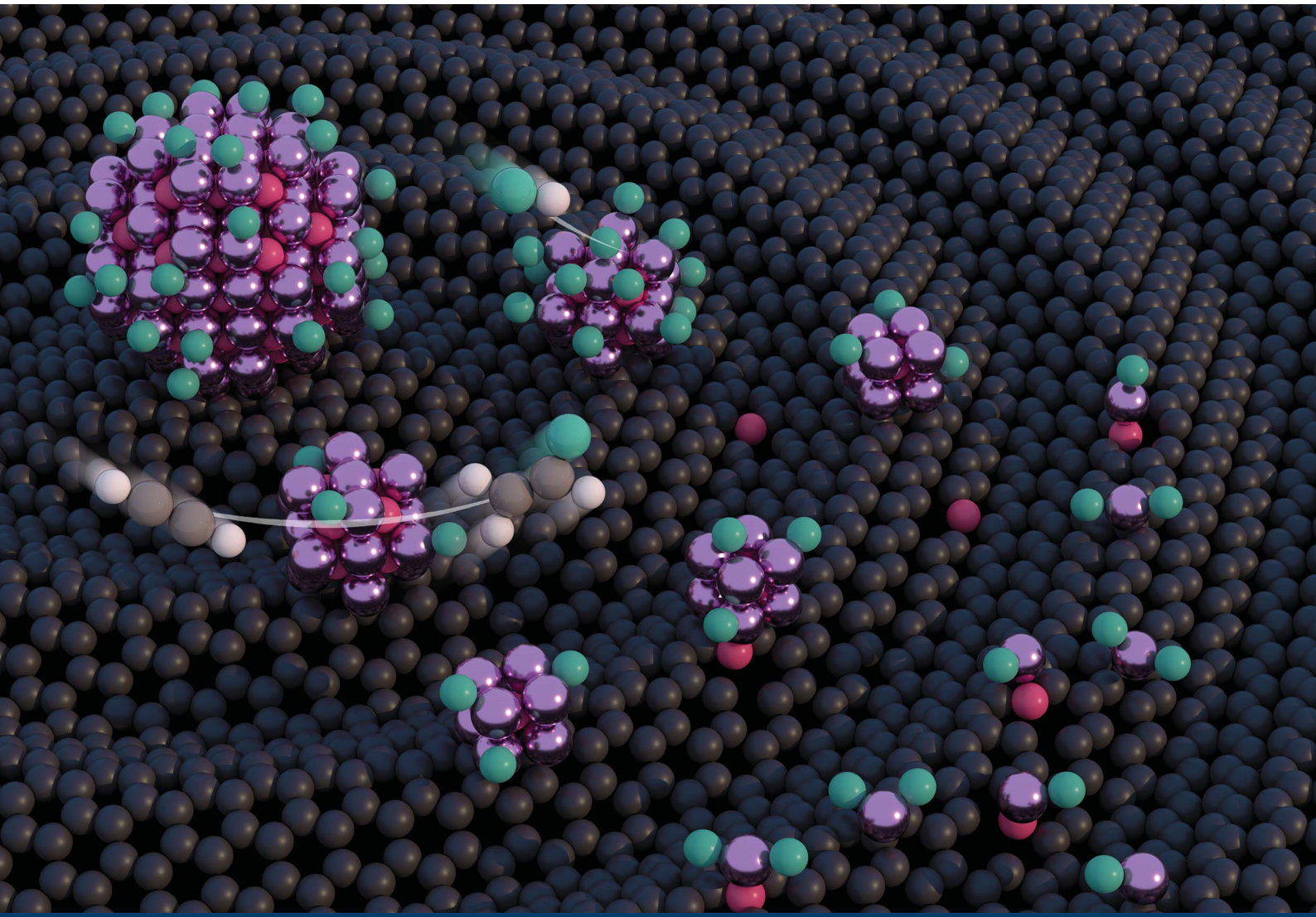

Themed issue: Single-Atom Catalysis

ISSN 2050-7488

ROYAL SOCIETY OF CHEMISTRY

**PAPER**

Javier Pérez-Ramírez *et al.*

Redispersion strategy for high-loading carbon-supported metal catalysts with controlled nuclearity

Journal of Materials Chemistry A

ROYAL SOCIETY OF CHEMISTRY

PAPER

View Article Online
View Journal | View Issue



Check for updates

Cite this: *J. Mater. Chem. A*, 2022, **10**, 5953

# Redispersion strategy for high-loading carbon-supported metal catalysts with controlled nuclearity†

Vera Giulimondi, [a] Selina K. Kaiser, [a] Mikhail Agrachev,[a] Frank Krumeich, [a] Adam H. Clark, [b] Sharon Mitchell, [a] Gunnar Jeschke[a] and Javier Pérez-Ramírez *[a]

Supported low-nuclearity metal catalysts integrating single atoms or small clusters have emerged as promising materials for diverse applications. While sophisticated synthetic methods provide a high level of nuclearity control in the subnanometre regime, these routes do not fulfil the requirements for translation into industrial practice of (i) effectiveness for high metal contents and (ii) facile scalability. Herein, we present a gas-phase redispersion strategy consisting of sequential $C_2H_2$ and HCl treatments to gradually disperse Ru, Rh and Ir nanoparticles supported on commercial activated carbon with metal content up to 10 wt% and initial average sizes of ≈ 1 nm into small clusters and eventually single atoms. Avoidance of nanoparticle surface overchlorination, which hinders $C_2H_2$ adsorption, is identified as key for the redispersion process, as demonstrated by the inefficacy of both $C_2H_2$–HCl cofeeding and inverse sequence (*i.e.*, HCl first) treatments. Precise size control (±0.1 nm) is enabled by regulating the number of $C_2H_2$–HCl cycles. Detailed characterisation by X-ray absorption spectroscopy, electron paramagnetic resonance and time-resolved mass spectrometry reveals that the redispersion occurs *via* a layer-by-layer mechanism. Specifically, the migration of surface chlorinated metal species to the carbon support is induced by the $C_2H_2$ treatment, depleting accessible surface Cl atoms, while the subsequent HCl treatment rechlorinates the cluster surface. The strategy paves the way for the generation of high-density metal sites with tuneable nuclearity for tailored applications.

Received 27th October 2021
Accepted 21st November 2021

DOI: 10.1039/d1ta09238c

rsc.li/materials-a

## 1. Introduction

Commercial heterogeneous catalysts frequently consist of supported highly dispersed metal species, targeting the maximal utilisation of the active component.[1] Aiming at full participation of metal nuclei in the catalytic cycle, research efforts have been directed towards low-nuclearity species, ranging from supported clusters of at most a few tens of atoms to single-atom catalysts (SACs).[2] Nanoscale engineering at the atomic level has demonstrated that the addition or removal of metal atoms to the active ensembles leads to distinct electronic properties and non-linear variation of reactivity patterns, often decisive to fulfil the catalytic cycle of the targeted application.[2–5] However, the exploitation of the unique reactivity of low-nuclearity catalysts in industrial practice calls for the development of scalable synthetic methods with control over speciation and nuclearity in the subnanometre regime. To this end, a number of strategies has been developed for supported clusters with controlled nuclearity including selected-precursor deposition,[6–8] support engineering,[9] wet chemical reduction[10] and dendrimer encapsulation.[11] Nevertheless, these methods face several challenges to avoid formation of large clusters and nanoparticles (NPs), thermodynamically favoured over low-nuclearity species, at high metal loadings, which are necessary to achieve industrially-suitable density of active sites.[2] Recently, remarkable progress has been achieved for the generation of high-loading single-atom catalysts (SACs). In particular, research efforts have been directed towards carbon supports, owing to their well-known ability to stabilise metal sites and tune their coordination environment.[12] Pioneering studies have reported advanced synthetic methods to stabilise isolated atoms with high metal content either (i) during the synthesis of the heteroatom-doped carbon supports *via* pyrolysis of organic precursors (10–16 wt%)[13] or functionalised graphene quantum dots (40 wt%),[14] or (ii) by wet chemistry methods exploiting existing hosts (18 wt%).[15] These strategies rely on generating suitable anchoring sites *via* the introduction of heteroatoms, defects and/or vacancies, but their applicability has not been

[a]*Institute for Chemical and Bioengineering, Department of Chemistry and Applied Biosciences, ETH Zurich, Vladimir-Prelog-Weg 1, 8093 Zurich, Switzerland. E-mail: jpr@chem.ethz.ch*

[b]*Paul Scherrer Institute, 5232 Villigen PSI, Switzerland*

† Electronic supplementary information (ESI) available. See DOI: 10.1039/d1ta09238c

demonstrated on practical supports,[16] which would be highly desirable to expand their versatility.

Redispersion methods of metal NPs on practical supports constitute a compelling alternative, simultaneously offering a potential route to precisely tune metal species nuclearity in the subnanometre regime until full atomic dispersion is achieved.[17] Several studies have demonstrated the efficacy of halogen-mediated strategies, namely chlorination, oxychlorination and halohydrocarbon-mediated treatments, generating $MO_xCl_y$ or $MCl_y$ species that redisperse *via* interaction with the support.[18] State-of-the-art studies have reported encouraging results on the efficacy of these strategies on metal loadings up to 5 wt% by synergistically coupling halohydrocarbons with compounds presenting lone pair electrons (*e.g.*, CO, NO or $O_2$), promoting the redispersion of the metal clusters by weakening the surface atom bonds to the cluster bulk *via* electron transfer.[19–21] These findings hold promise for exciting prospects, calling for the exploration of other classes of promoters for halogen-mediated strategies, among which mildly-reducing compounds emerge as potentially effective candidates to cleave bonds in metal clusters.[22] To this end, a promising pair may be identified in HCl and $C_2H_2$, on the basis of literature-reported Ru NPs supported on N-doped carbon that were atomically redispersed under $C_2H_2$ hydrochlorination conditions.[23] Nevertheless, in that case competitive particle agglomeration was observed, resulting in lack of control over the redispersion process. To date, this remains a critical challenge that, if resolved, could pave the way towards a scalable strategy for the generation of high loading metal catalysts on commercial supports with tuneable nuclearity.

Herein, we present a scalable redispersion strategy, consisting of sequential $C_2H_2$ and HCl treatments, to synthesise Ru, Ir and Rh catalysts with metal loading up to 10 wt% on N-doped and commercial activated carbons with controlled metal nuclearity in the subnanometre regime down to atomic dispersion. Fine control over the metal species nuclearity is enabled by regulation of the number of $C_2H_2$–HCl cycles. The inefficacy of both the $C_2H_2$–HCl cofeeding and inverse sequence (*i.e.*, HCl first) approaches demonstrates the beneficial impact of avoiding NP surface overchlorination, which prevents the adsorption of $C_2H_2$. By combination of microscopic, spectroscopic and spectrometric analyses, the redispersion mechanism is revealed to be a layer-by-layer process in which $C_2H_2$ prompts the migration of chlorinated metal species from the nanoparticle surface onto local defects in the carbon support, while HCl chlorinates the newly exposed metal atoms. This work presents a potentially industrially-amenable route to generate carbon-supported metal species with tuneable nuclearity for tailored catalytic applications.

# 2. Experimental

## 2.1 Metal NP synthesis

Commercial activated carbon (AC, Norit ROX 0.8) was ground and sieved (particle size 0.4–0.6 mm). The N-doped carbon support (NC) was prepared in a two-step synthesis, consisting of an oxidative polymerisation of aniline and a subsequent carbonisation step.[24] Aniline (50 mmol, Acros, 99.5%) was dissolved in deionised water (40 $cm^3$, pH 0.4; adjusted by hydrochloric acid, 1.25 M, Sigma Aldrich, >37%) at room temperature, cooled to 277 K, and subsequently added to a precooled solution (277 K) of ammonium persulfate (50 mmol, Acros, 98%) in deionised water (20 $cm^3$). After vigorous manual stirring (5 min), the mixture was kept at room temperature for 24 h to complete the polymerisation process. The formed polyaniline was thoroughly washed with deionised water for neutralisation, dried in vacuum (393 K, heating rate 5 K $min^{-1}$, hold time 12 h), and afterwards treated at 1073 K (heating rate 5 K $min^{-1}$, hold time 1 h, static $N_2$). The obtained N-doped carbon, having a N content of 9.7 wt% and a total surface area of $S_{BET}$ = 517 $m^2$ $g^{-1}$, was ground and sieved (particle size 0.4–0.6 mm). All metal-based catalysts were prepared *via* an incipient wetness impregnation method with a nominal metal loading of 10 wt%. The desired metal precursor, $RuCl_3 \cdot xH_2O$ (ABCR, 99.9%, 40.0 wt% Ru), $IrCl_3 \cdot xH_2O$ (ABCR, 99.9%, 65 wt% Ir) or $RhCl_3 \cdot xH_2O$ (Acros Organics, 99.9%, 38 wt% Rh), was dissolved in water (1.5 $cm^3$ $g^{-1}$) and the obtained solution was added dropwise to the selected carbon carrier (AC or NC). Subsequently, the samples were dried (473 K, heating rate 5 K $min^{-1}$, hold time 12 h, static air) to yield the nanoparticle catalysts, denoted as 10M/AC or 10M/NC. The prereducing treatment was carried out at 573 K (heating rate 10 K $min^{-1}$, hold time 3 h), flowing pure $H_2$ (PanGas, purity 5.0) at a total volumetric flow of $F_T$ = 40 $cm^3$ STP $min^{-1}$.

## 2.2 Redispersion treatment

The redispersion treatment was conducted at atmospheric pressure in a continuous-flow fixed-bed micro-reactor (Scheme S1†). The gases $C_2H_2$ (PanGas, purity 2.6), HCl (Air Liquide, purity 2.8, anhydrous), Ar (PanGas, purity 5.0, internal standard) and He (PanGas, purity 5.0, carrier gas), were fed using digital mass-flow controllers (Bronkhorst) to the mixing unit, equipped with a pressure indicator. A quartz micro-reactor (10 mm inner diameter) was loaded with the catalyst ($W_{cat}$ = 0.1 g, particle size 0.4–0.6 mm) and placed in a homemade electrical oven. A K-type thermocouple fixed in a coaxial quartz thermowell with the tip positioned in the centre of the catalyst bed was used to control the temperature during the redispersion treatment. Prior to treatment, the catalyst was heated in a He flow to the desired temperature ($T$ = 473 K) and allowed to stabilise for at least 30 min before the gas mixture was fed (total volumetric flow, $F_T$ = 15 $cm^3$ STP $min^{-1}$). The sequence for each cycle consisted of (i) exposure to $C_2H_2$ atmosphere for 1 h (40 vol% $C_2H_2$, 44 vol% He and 16 vol% Ar), (ii) He flushing for 5 min (84 vol% He and 16 vol% Ar), (iii) exposure to HCl atmosphere for 1 h (44 vol% HCl, 40 vol% He and 16 vol% Ar) and (iv) He flushing for 5 min (84 vol% He and 16 vol% Ar). The treated samples are denoted as 10M/C X where M: metal, C: "AC" or "NC", X: # of $C_2H_2$–HCl treatment cycles and y: "a" if the cycle terminated after the $C_2H_2$ treatment. Time-resolved mass spectroscopy (MS) analysis of the reactor outlet stream was performed with a Pfeiffer Vacuum Thermo-Star GDS 320 T1 MS

 

to monitor the relative concentration of produced vinyl chloride ($C_2H_3Cl$, VCM) with $m/z$ 62 and $m/z$ 64. In line with the natural isotopic abundance of $^{35}Cl$ and $^{37}Cl$, $m/z$ 62 and $m/z$ 64 were detected in a characteristic 3 : 1 ratio.

### 2.3 Characterisation

Inductively coupled plasma optical emission spectrometry (ICP-OES) was conducted using a Horiba Ultra 2 instrument equipped with photomultiplier tube detection. The solids were dissolved in a 3 : 1-mixture of $HNO_3$ and $H_2O_2$ under sonication until the absence of visible solids. Powder X-ray diffraction (XRD) was measured using a PANalytical X'Pert PRO-MPD diffractometer with Cu-K$\alpha$ radiation ($\lambda = 1.54060$ Å). The data was recorded in the 10–70° $2\theta$ range with an angular step size of 0.017° and a counting time of 0.26 s per step. Scanning transmission electron microscopy (STEM) with a high-angle annular dark-field (HAADF) detector was performed on an aberration-corrected HD2700CS (Hitachi) microscope operated at 200 kV. High-resolution transmission electron microscopy (HRTEM) was performed on a double-corrected microscope JEM-ARM300F (GrandARM, JEOL), which was operated at an acceleration potential of $U_{acc} = 300$ kV (electron gun: cold-field emitter; $\Delta E \approx 0.35$ eV). Static volumetric chemisorption of acetylene was performed in a Micromeritics 3Flex Chemi instrument at 303 K. Energy-dispersive X-ray spectroscopy was conducted in a Talos F200X instrument with an FEI SuperX detector at 200 kV. Image frame times ranged from 20 to 40 µs (512 × 512 px). Samples were prepared by dipping the copper grid supporting a holey carbon foil in a suspension of the solid in ethanol and drying in air. The Ir 4f and Rh 3d X-ray photoelectron spectroscopy (XPS) spectra of the Ir and Rh samples were acquired on a Physical Electronics Quantera SXM instrument using monochromatic Al-K$\alpha$ radiation, generated from an electron beam operated at 15 kV, and equipped with a hemispherical capacitor electron-energy analyser. The samples were analysed at an electron take-off angle of 45° and a constant analyser pass energy of 55 eV. Owing the Ru 3d core levels superimposing the C 1s core level, the Ru speciation was analysed based on Ru 3p XPS spectra.[25] The Ru 3p XPS spectra of the Ru samples were acquired on a Physical Electronics Quantum 2000 instrument, where the samples were analysed at an electron take-off angle of 45° and a constant analyser pass energy of 46.95 eV. Both spectrometers were calibrated for the Au $4f_{7/2}$ signal at 84.0 ± 0.1 eV. The Ru 3p and Rh 3d XPS spectra were fitted by mixed Gaussian–Lorentzian and the Ir 4f XPS spectra were fitted by Functional Lorentzian component profiles after Shirley background subtraction. The selected peak positions are based on literature data and fixed with an error of ±0.2 eV. The detailed fitting parameters are given in the ESI.† The elemental concentrations were quantified based on the measured photoelectron peak areas (C 1s, N 1s, O 1s, Cl 2p, Ru 3p, Ir 4f and Rh 3d), using the respective photoionisation cross sections as relative sensitivity factors.[26] X-ray absorption fine structure (XAFS) measurements were carried out at the SuperXAS beamline of the Swiss Light Source.[27] The incident photon beam was provided by a 2.9 T superbend magnet and subsequently collimated using a Pt-coating (for the Ru K edge). The rejection of higher harmonics and focusing were achieved with a Rh-coating (for Ir $L_3$ edge) and a Pt-coating (for Ru K and Rh K edges), respectively. The beamline was calibrated using the respective metal foils. The sample area illuminated by the X-ray beam was 0.5 mm × 0.2 mm. All spectra were recorded in transmission mode at room temperature. The extended X-ray absorption fine structure (EXAFS) spectra were acquired with a 1 Hz frequency (0.5 s per spectrum) and then averaged over 5 min. The resulting raw data were processed using the ProQEXAFS software,[28] and the EXAFS spectra were analysed using the Demeter software.[29] Hydrogen temperature-programmed reduction analyses ($H_2$-TPR) were performed in a Micromeritics Autochem II 2920 analyser equipped with a thermal conductivity detector (TCD). Peaks in the TCD signal are assigned based on reference values in the literature.[30,31] Continuous wave (CW) electron paramagnetic resonance (EPR) spectroscopy experiments were performed at 10 K on a Bruker Elexsys E500 spectrometer equipped with an Oxford helium (ESR900) cryostat operating at X-band frequencies (≈9.4 GHz) using a ER4122SHQE Bruker EPR Resonator. All CW EPR spectra were acquired (spectrometer settings: microwave frequency = 9.4 GHz, center field = 330 mT, sweep width = 200 mT, modulation frequency = 100 kHz, microwave power = 207 µW, power attenuation = 30 dB, conversion time = 327.68 ms, time constant = 81.92 ms), while all measured $g$-factors were offset-corrected against a known standard (*i.e.*, free radical 1,1-diphenyl-2-picrylhydrazyl). The EPR spectra were simulated on Matlab using the Easyspin software.[32] The positions of spectral features in EPR spectra are defined by the principal values of the $g$-tensor: a single $g$-factor for the isotropic case, $g_{xx}$, $g_{yy}$ and $g_{zz}$ for the orthorhombic case, $g_{II}$ and $g_{\perp}$ for the axial case. Specifically, for a low spin d5 ion in a tetragonally distorted site (like signal Ru–Cl), it is possible to quantitatively relate the principal values of the $g$-factor with crystal field parameters through the following equations:[33]

$$g_{II} = g_e(a^2 - b^2) - kb^2 \quad (1)$$

$$g_{\perp} = g_e a^2 + 2\sqrt{2}kab \quad (2)$$

$$a = \frac{1}{\sqrt{2}}\left[1 + \frac{\eta - \frac{1}{2}}{\left(\eta^2 - \eta + \frac{9}{4}\right)^{1/2}}\right]^{1/2} \quad (3)$$

$$b = \frac{1}{\sqrt{2}}\left[1 - \frac{\eta - \frac{1}{2}}{\left(\eta^2 - \eta + \frac{9}{4}\right)^{1/2}}\right]^{1/2} \quad (4)$$

$$\eta = \frac{\delta}{\zeta} \quad (5)$$

where $g_e$: the free electron $g$-factor ($g_e = 2.0023$), $k$: the orbital reduction factor, $\delta$: is the splitting of the $t_{2g}(0)$ and $t_{2g}(\pm 1)$ energy levels induced by the tetragonal crystal field and $\zeta$: the

one-electron spin–orbit coupling constant, which can be assumed independent on structural changes in the $Ru^{III}$ environment. $\eta$ is therefore directly proportional to the crystal field splitting. The increase of $\eta$ with the number of $C_2H_2$–HCl treatment cycles agrees with our interpretation as discussed in the results and discussion section (*vide infra*, Section 3.2.1). The best fit was obtained for $k = 1$.

# 3. Results and discussion

## 3.1 Controlled redispersion of carbon-supported Ru NPs

**3.1.1 Development of the redispersion strategy.** Carbon-supported Ru NPs were first synthesised by simple incipient wetness impregnation of AC and NC with aqueous solutions of $RuCl_3 \cdot xH_2O$ (nominal metal loading of 10 wt% confirmed by ICP-OES, Table S1†) and thermally activated at 473 K (see experimental section, sample code: 10Ru/AC and 10Ru/NC, respectively). In an effort to overcome the current limitations in the effectiveness of halogen-mediated redispersion methods, a potential solution may consist in promoting the effect of the selected halogen compound with a mildly-reducing agent.[18] To this end, $C_2H_2$ and HCl were identified as a promising pair, prompted by the previously-reported redispersion of NC-supported Ru NPs into single atoms induced by simultaneous exposure to both gases (cofeeding) that is, yet, ineffective for Ru NPs supported on commercial AC due to the weaker anchoring properties of O-functionalities compared to N-functionalities.[34] However, owing to lack of control over the redispersion driving force, the cofeeding approach could not lead to atomic dispersion of NC-supported Ru NPs upon increasing the metal content (from 5 wt% to 10 wt%, Fig. 1 and S1†), even with prolonged treatment durations (from 12 to 50 h, Fig. S1†). To overcome this limitation, a new approach was explored aiming to (i) decouple, (ii) control and (iii) maximise the effect of each gas in the process. Therefore, the Ru NPs were sequentially exposed to HCl and $C_2H_2$ atmospheres and *vice versa*. The treatment conditions were selected to achieve equivalent exposure to each molecule as experienced when $C_2H_2$ and HCl were cofed. While treatment with HCl first did not affect the size of the Ru NPs, exposure to $C_2H_2$ first resulted in partial redispersion. This observation reveals the central role of avoiding competitive adsorption of the two gases, which presumably leads to surface overchlorination preventing adsorption of $C_2H_2$,[35] in gaining control over the process. Furthermore, the partial redispersion observed in the latter case hints at a surface layer removal of Ru species, suggesting that multiple $C_2H_2$–HCl treatment cycles may be required to fully disperse NPs into isolated atoms. On the basis of these findings, a new strategy was developed, consisting of cyclic exposure of Ru NPs to alternating (1 h) $C_2H_2$ and HCl atmospheres. Strikingly, not only does this strategy achieve atomic dispersion on both NC and commercial AC, as visualised in HAADF-STEM analysis (Fig. 2, S1 and S2†), but it also enables gradual and controlled NP redispersion, as reflected in the evaluation of the average cluster size at different stages of the treatment (Fig. 2, sample code: 10M/C-X where M: metal, C: "AC" or "NC", X: # of $C_2H_2$–HCl treatment cycles and y: "a" if the cycle terminated after the $C_2H_2$ treatment). In stark contrast to the previously-reported methods, which could modulate the reduction in the NP size in the nanometre regime,[36] the presented strategy enables finely-resolved control over the redispersion process to the subnanometre regime, tuning the metal nuclearity by regulating the number of $C_2H_2$–HCl treatment cycles.

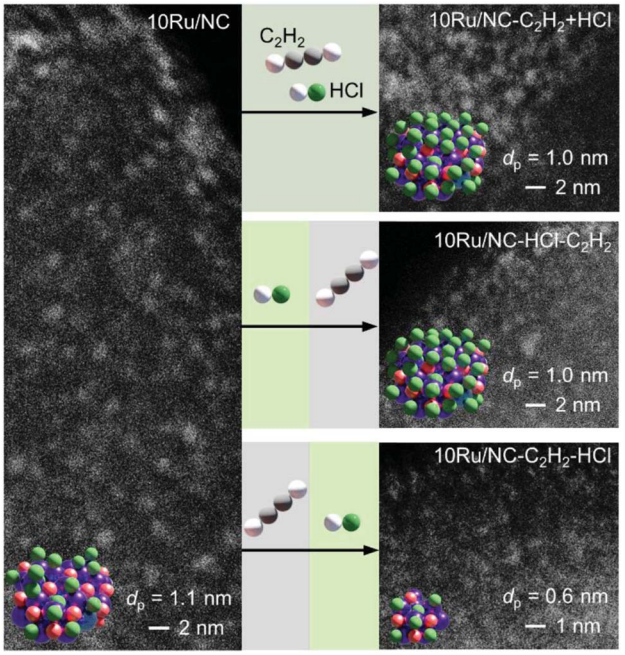


Fig. 1 HAADF-STEM images of 10Ru/NC, in fresh and treated forms, indicating the average metal particle size ($d_p$). The graphical representation of the different samples (colour code: purple = Ru, red = O and green = Cl) show the effect of different redispersion treatments: $C_2H_2$–HCl cofeeding for 12 h (10Ru/NC-12h, ineffective in the redispersion of the Ru NPs) and sequential HCl and $C_2H_2$ atmosphere for 6 h each (10Ru/NC-HCl-$C_2H_2$) likely resulting in overchlorinated Ru NPs as well as sequential $C_2H_2$ and HCl atmospheres for 6 h each (10Ru/NC-$C_2H_2$–HCl) leading to partial redispersion. Treatment conditions: $W_{cat} = 0.1$ g, $F_T = 15$ cm$^3$ STP min$^{-1}$, $T = 473$ K, cofeeding: 40 vol% $C_2H_2$, 44 vol% HCl, 16 vol% Ar, $C_2H_2$ exposure: 40 vol% $C_2H_2$, 44 vol% He, 16 vol% Ar and HCl exposure: 44 vol% HCl, 40 vol% He, 16 vol% Ar.

**3.1.2 Role of Cl surface atoms of fresh nanoparticles in the redispersion process.** Owing to the small size of Ru clusters, below the resolution of XRD (≤1 nm, Fig. S3†), their structural characterisation mainly relies on EXAFS (Fig. 3a and S4, Tables S2 and S3†). Interestingly, no pronounced metallic contributions were observed, suggesting a metal oxychloride architecture, $RuO_xCl_y$, where Ru atoms are bridged by O atoms. To explore the role of Cl ligands in the redispersion process, the Ru NPs were prereduced under a $H_2$ atmosphere, 10Ru/AC-R, keeping the temperature lower than 673 K to remove surface Cl atoms while preventing $RuO_x$ reduction to metallic Ru.[34] Accordingly, the chlorination degree was markedly reduced (Ru–Cl CN = 2.0 and CN = 0.9 in 10Ru/AC and 10Ru/AC-R, respectively) and the sample acquired an enhanced metallic character CN = 0.2 and CN = 1.2 in 10Ru/AC and 10Ru/AC-R, respectively). Owing to the limitation of EXAFS in

 

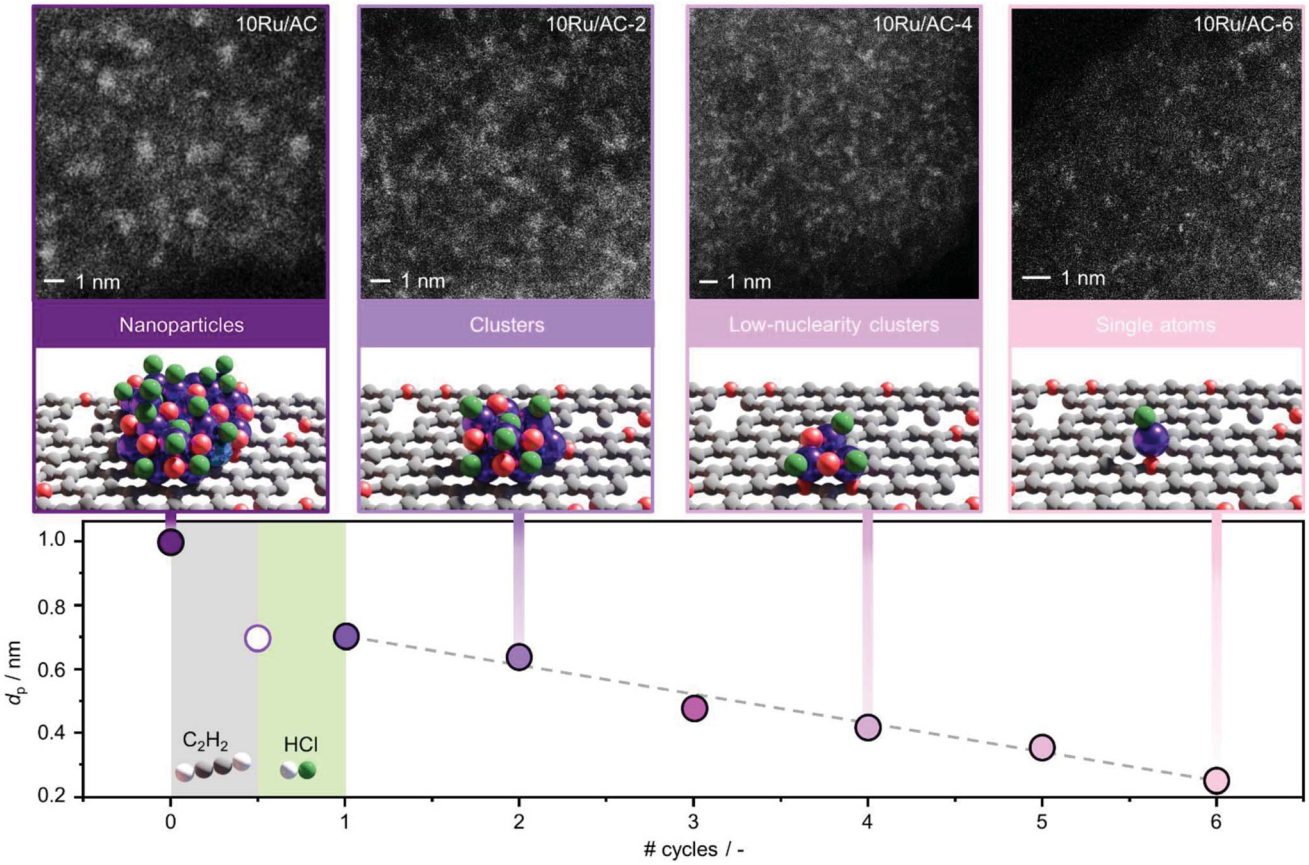


Fig. 2 Average metal particle size ($d_p$) of 10Ru/AC, in fresh and treated forms, as a function of the number of $C_2H_2$–HCl treatment cycles and HAADF-STEM images of selected samples, visualising the control over nuclearity enabled by the redispersion treatment. One cycle consists of exposure to $C_2H_2$ atmosphere followed by exposure to HCl atmosphere, for 1 h each. Treatment conditions: $W_{cat} = 0.1$ g, $F_T = 15$ cm$^3$ STP min$^{-1}$, $T = 473$ K, $C_2H_2$ treatment: 40 vol% $C_2H_2$, 44 vol% He, 16 vol%, Ar, HCl treatment: 44 vol% HCl, 40 vol% He, 16 vol% Ar.

distinguishing between Ru–O and Ru–C bonds, more accurate information on the impact of the prereducing treatment on $RuO_x$ species was acquired by $H_2$-TPR analysis of 10Ru/AC and 10Ru/AC-R, showing that $RuO_x$ species were substantially preserved (Fig. 3d). Notably, the removal of surface Cl atoms inhibited the NP redispersion (Fig. S5†), indicating their pivotal role in the process by forming mobile $RuO_xCl_y$ species.[18,23]

**3.1.3 Evolution of the metal nuclearity.** Insights on the generated cluster speciation were gained by means of XPS and XAS analyses, conducted on 10Ru/AC samples after consecutive $C_2H_2$–HCl treatment cycles. In line with the XANES results (Fig. S6†), the Ru 3p XPS spectra progressively assume a more oxidised character (Fig. 3b, Table S4†). Owing to the oxychloride architecture of the Ru clusters, where Ru–Ru interactions are weak, information on their nuclearity from EXAFS relies on other coordination shells. Remarkably, two distinct Ru–O/C fingerprints are identified upon fitting the EXAFS spectra of 10Ru/AC in both fresh and treated forms (Fig. S7, Table S2†): (i) short-bonding Ru–O/C contributions at $R = 1.83$ Å ascribable to $RuO_xCl_y$ species in the clusters,[37] and (ii) long-bonding Ru–O/C contributions at $R = 2.2$ Å likely reflecting metal-support interactions, possibly of carbide nature.[38] The evolution of the metal nuclearity over the course of the treatment thus manifests in progressively decreasing short-bonding Ru–O/C interactions (CN = 0.9 and CN = 0.5 in 10Ru/AC and 10Ru/AC-6, respectively), contrasted by more prominent long-bonding Ru–O/C interactions (CN = 2.4 and CN = 4.7 in 10Ru/AC and 10Ru/AC-6, respectively). Additionally, in agreement with XPS analysis and the weaker adsorption of HCl on Ru single atoms compared to NPs,[35] the redispersed Ru species present a lesser chlorinated character (Ru–Cl CN = 2.0 and CN = 1.5 in 10Ru/AC and 10Ru/AC-6, respectively).

### 3.2 Redispersion mechanism

**3.2.1 Contributions of $C_2H_2$ and HCl to the redispersion process.** To probe the role of each gas in the redispersion process, a comparative analysis was conducted between prolonged exposure (12 h) of 10Ru/AC solely to $C_2H_2$ and HCl. Remarkably, HAADF-STEM analysis revealed that only $C_2H_2$ promotes the process, leading to partial redispersion ($\approx$0.4 nm), while exposure to HCl leaves the NP size unaltered (Fig. S5†). However, it should be noted that atomic dispersion could not be achieved with sole $C_2H_2$, likely limited from depletion of the originally present surface Cl atoms. Consistently, analysis of the Ru K edge EXAFS spectra show stronger long-bonding Ru–O/C interactions in 10Ru/AC-1a compared to

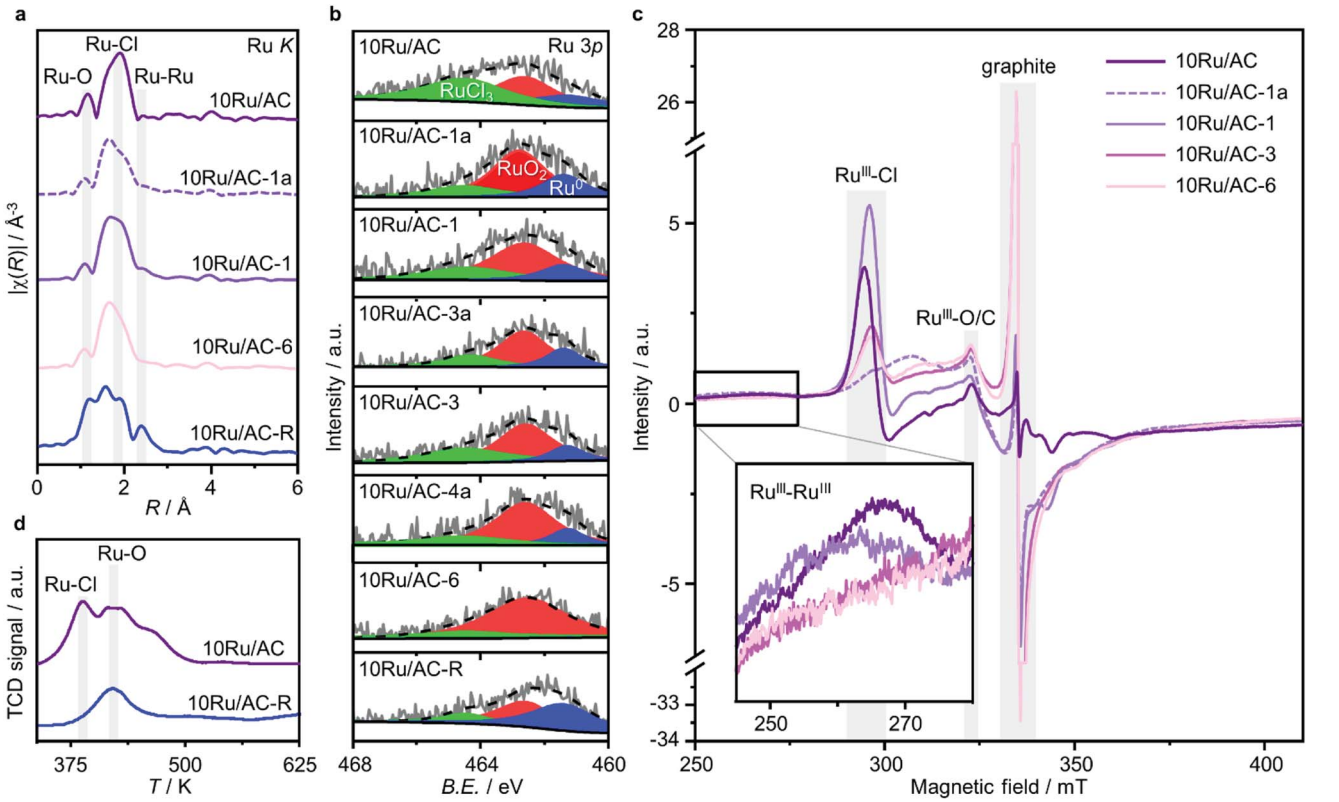


Fig. 3 Characterisation of 10Ru/AC, in fresh and treated forms, resolving the roles of $C_2H_2$ and HCl in the redispersion process. (a) Ru K edge spectra showing progressively stronger Ru–O/C and weaker Ru–Cl interactions, (b) Ru 3p XPS spectra evidencing increasingly prominent oxidised character and (c) EPR spectra exhibiting (i) three different contributions to the $Ru^{III}$ signal, showing increasing anisotropy and weaker $Ru^{III}$–$Ru^{III}$ interactions over the course of the treatment, as well as (ii) a graphite signal evidencing a progressively increase in local defect on graphitic carbon phases in the support. (d) $H_2$-TPR profiles of 10Ru/AC and 10Ru/AC-R, showing significant loss in the Ru–Cl peak upon reduction, in line with the metallic Ru character detected in both the Ru K edge and Ru 3p XPS spectra of the reduced sample.

10Ru/AC (CN = 4.1 and CN = 2.4, respectively), complemented by weaker short-bonding ones (CN = 0.5 and CN = 0.9, respectively) and a simultaneous loss in Ru–Cl coordination (CN = 1.4 and CN = 2.0, respectively), which is partially recovered upon exposure to HCl (CN = 1.9 in 10Ru/AC-1) while both the long-bonding and the short-bonding Ru–O/C interactions remain substantially unaffected (CN = 4.1 and CN = 0.5 in 10Ru/AC-1a and CN = 4.2 and CN = 0.6 in 10Ru/AC-1, respectively). Accordingly, comparison of the Ru 3p XPS spectra of 10Ru/AC-1 and 10Ru/AC-1a, as well as of 10Ru/AC-3 and 10Ru/AC-4a (*i.e.*, at later stages of the redispersion treatment), indicates formation of new chlorinated Ru species on the surface of the metal cluster occurring *via* oxidative Cl-addition under HCl atmosphere. Conversely, comparison of the Ru 3p XPS spectra of 10Ru/AC-1a and 10Ru/AC, as well as of 10Ru/AC-4a and 10Ru/AC-3, shows a mildly reducing effect of $C_2H_2$, mainly resulting in the removal of the surface Cl atoms in the metal cluster.

These results were further corroborated by EPR analysis, simultaneously providing additional insights on the progressively stronger interaction of the Ru species with the support. Owing to the non-Kramers nature of $Ru^0$ and $Ru^{IV}$ species, EPR only detects $Ru^{III}$ species, presenting a low-spin $d^5$ configuration that gives rise to one unpaired electron ($s = 1/2$). These can be fitted by a weighted sum of four contributions (Fig. 3c and S8, Table S5†): (i) a broad anisotropic signal with axial *g*-factor ascribed to $Ru^{III}$ mainly coordinated by Cl (weak-field coordinating atoms) in an tetragonally distorted geometry ($g_\perp = 2.265$ and $g_{II} = 1.95$, $Ru^{III}$–Cl signal), (ii) another anisotropic signal with rhombic *g*-factor attributed to $Ru^{III}$ mainly coordinated by O and C (strong-field coordinating atoms) ($g_{xx} = 2.08$, $g_{yy} = 1.99$, $g_{zz} = 1.865$, $Ru^{III}$–O/C signal), (iii) a very broad signal, assigned to $Ru^{III}$ ions interacting in relatively large clusters ($g \approx 2.15$, $Ru^{III}$–$Ru^{III}$ signal), as well as (iv) an additional sharp signal with isotropic *g*-factor, typical of delocalised electrons in graphitic carbon structures ($g = 2.0048$, graphitic carbon signal).[39,40] In agreement with EXAFS and XPS analyses, the intensity of the $Ru^{III}$–Cl signal in 10Ru/AC dramatically decreases upon exposure to $C_2H_2$, 10Ru/AC-1a, regaining prominence upon exposure to HCl, 10Ru/AC-1. Compared to 10Ru/AC, the $Ru^{III}$–Cl signal in 10Ru/AC-1 is stronger, evidencing chlorination of an increased number of metal sites resulting from the higher dispersion degree and lower anisotropy, reflected by a shift towards higher magnetic field and indicative of a lower chlorination degree in the redispersed metal sites. After the first cycle, the cluster anisotropy gradually decreases over consecutive treatments, resulting in a stronger crystal field induced by higher coordination with the O or C functionalities in the support (*i.e.*, increasing $\eta$, see experimental section, Fig. S9a†). The signal

 

intensity progressively reduces in favour of increasing intensity of the $Ru^{III}$–O/C signal (Fig. S9b†). In line with this, $Ru^{III}$–$Ru^{III}$ interactions are no longer detected in the spectra of either 10Ru/AC-3 or 10RuAC-6. Intriguingly, the stronger interaction of the Ru species with the support also reflects in the more prominent graphitic carbon signal, ascribed to local defects in graphitic carbon structures that originate from exposure to $C_2H_2$ and presumably serve as anchoring sites for the mobile $RuO_xCl_y$ species (Fig. 3d and S9c†). Owing to the known ability of Ru to form graphitic carbon layers,[23] HRTEM analysis was conducted to verify the accessibility of the metal sites, but no evidence of encapsulation of Ru clusters is visible (Fig. S10†), which is consistent with the similar surface metal content in 10Ru/AC and 10Ru/AC-6 detected in XPS (Table S6†). Notably, the EPR spectra of 10Ru/AC-R, prereduced under a $H_2$ atmosphere, and 10Ru/AC-R-6, where the redispersion is inhibited, exhibit similar graphitic carbon signals (Fig. S8†), further corroborating the important role of the local defects in the process.

**3.2.2 $C_2H_2$ adsorption as descriptor for the redispersion process.** Consistent with the reported superior catalytic activity of $RuO_xCl_y$ NPs compared to Ru single atoms in the $C_2H_2$ hydrochlorination reaction for VCM production,[23] the $C_2H_2$ adsorption capacity, identified as a key descriptor for the performance,[41] decreases with increasing Ru dispersion (also reflected in decreasing VCM evolution during the treatment, *vide infra*, Fig. 4). Accordingly, the $C_2H_2$ adsorption capacity only marginally increases upon exposure to HCl, which leaves the cluster size unaltered, presumably due to the desorption of some residual acetylene molecules. To explore the dynamics of the redispersion process, the reactor outlet stream was analysed by time-resolved MS. During the $C_2H_2$ treatments, the $C_2H_2$ signal rapidly rises and gradually stabilises, indicating initial adsorption and subsequent conversion into VCM. Intriguingly, the sharp maximum in the VCM signal is followed by a delayed, broader $O_2$ signal whose maximum occurs after VCM is almost fully depleted. Following the $O_2$ evolution, no more VCM is detected, in line with the steady-state $C_2H_2$ signal, clearly indicating complete exhaustion of the accessible Cl atoms initially present on the cluster surface, which will require exposure to HCl for rechlorination. These findings enable delineation of a layer-by-layer redispersion mechanism, consisting of the following steps: (i) the $C_2H_2$-induced removal of surface Cl atoms *via* VCM evolution, (ii) the generation of undercoordinated $RuO_xCl_y$ species migrating from the original Ru cluster onto defects in the carbon support, possibly promoted by the exothermicity of the $C_2H_2$ hydrochlorination reaction, (iii) the coupling of undercoordinated surface O atoms presumably originating from $RuO_xCl_y$ species detachment (leading to the formation and evolution of $O_2$) and (iv) the rechlorination of cluster surface upon exposure to HCl (Fig. 5). The high aptitude of $RuO_x$ species to be chlorinated agrees with previous density functional theory simulations on carbon-supported $RuO_x$ NPs.[35] Furthermore, adsorption energies of $C_2H_2$, −189 kJ $mol^{-1}$, and HCl, −255 kJ $mol^{-1}$, computed by density functional theory,[35] explain the importance of avoiding competitive adsorption in the process. Specifically, the dominant adsorption properties of HCl over $C_2H_2$ suggest that in the presence of both gases the evolution of VCM would be followed by immediate rechlorination, inhibiting the redispersion process by hindering the adsorption of $C_2H_2$ and thus the formation of the mobile $RuO_xCl_y$ species.

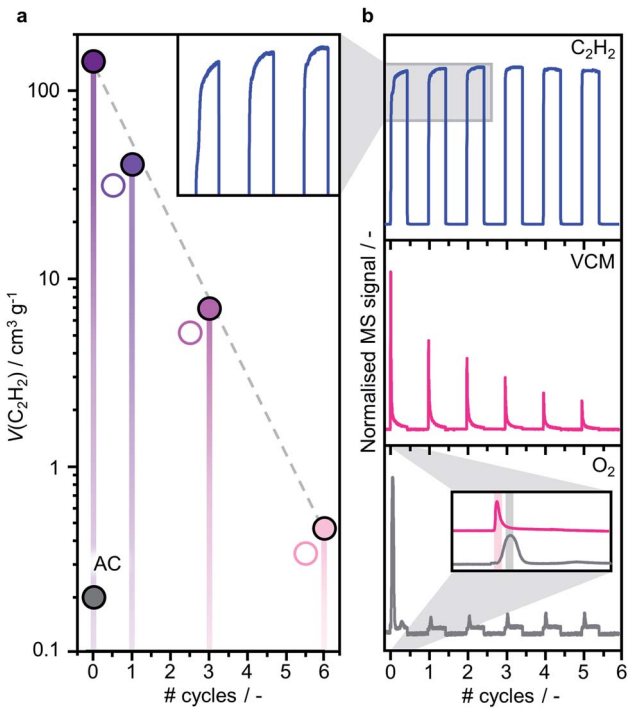


Fig. 4 (a) $C_2H_2$ adsorption capacity determined by chemisorption analysis of 10Ru/AC, fresh and after consecutive $C_2H_2$–HCl treatment cycles, and (b) time-resolved MS product analysis, showing the evolution of peaks associated to $C_2H_2$, VCM and $O_2$ during the $C_2H_2$–HCl treatment cycles. The decreasing trend in the $C_2H_2$ adsorption capacity of the samples agrees with the $C_2H_2$ signal in the product analysis, exhibiting progressively shorter time required for stabilisation (as shown in the inset).

### 3.3 Extrapolation to other metals

Encouraged by the controllability and scalability, we explored the effectiveness of the redispersion strategy for supported Ir and Rh catalysts. Remarkably, not only was atomic dispersion achieved in both cases at 10 wt% loading, but the same fine control over nuclearity was enabled by regulation of the number of $C_2H_2$–HCl treatment cycles (Fig. 6, S11 and S12†). As for the Ru NP catalysts, no prominent metallic character was observed for either Ir or Rh NPs in either XPS or XAS (Fig. S13 and S14, Tables S3, S7 and S8†), likely due to the high affinity of these metals for Cl (M–Cl CN = 5.1 and CN = 4.4 in 10Ir/AC and 10Rh/AC, respectively). However, in contrast to 10Ru/AC, no short-bonding M–O/C contributions could be identified, suggesting a metal chloride architecture and further corroborating the key role of mobile metal chloride species in the redispersion process. In line with the XPS analysis, showing dechlorination and a more oxidic character (Fig. S13, Tables S7 and S8†), the metal-support interaction with the support becomes more

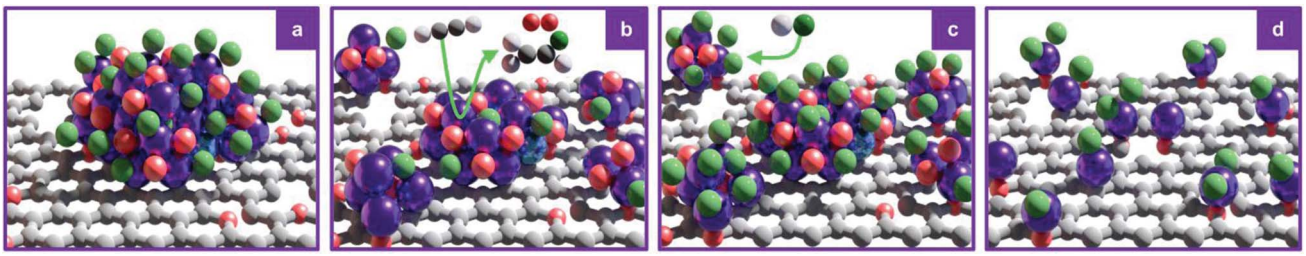


Fig. 5 Schematic representation of the $C_2H_2$-induced redispersion mechanism of (a) $RuO_xCl_y$ NPs supported on carbon. (b) $C_2H_2$ reduces the NP surface, evolving VCM, depleting accessible surface Cl atoms, and $O_2$ while promoting Ru redispersion into smaller clusters or atoms. (c) Exposure to HCl leads to oxidative Cl addition, rechlorinating the cluster surface. (d) The alternating treatment is effective until full atomic dispersion is achieved. Colour code: purple = Ru, red = O, green = Cl, grey = C and white = H.

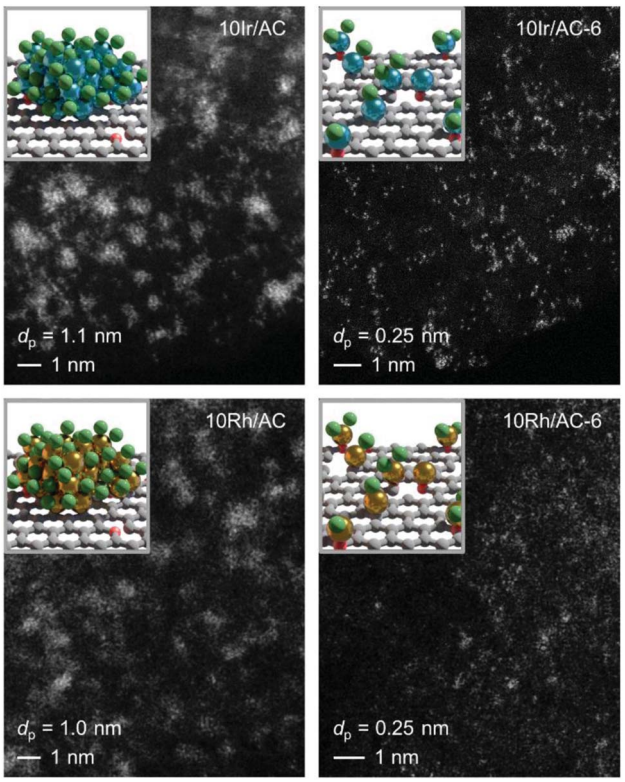


Fig. 6 Successful extrapolation of the redispersion treatment to supported Ir and Rh catalysts. HAADF-STEM images of 10Ir/AC and 10Rh/AC, in fresh and treated forms, together with average particle size ($d_p$). Atomic dispersion is visualised in 10Ir/AC-6 and 10Rh/AC-6.

prominent in the atomically redispersed species (Ir–O/C CN = 0.7 and CN = 1.6 in 10Ir/AC and 10Ir/AC-6, respectively, and Rh–O/C CN = 2.5 and CN = 4.0 in 10Rh/AC and 10Rh/AC-6, respectively), while the M–Cl interactions decrease (Ir–Cl CN = 3.6 in 10Ir/AC-6 and Rh–Cl CN = 1.6 in 10Rh/AC-6). These results hold promise for the general applicability of the redispersion strategy to a broad range of metals.

## 4. Conclusions and outlook

In summary, our study demonstrated a redispersion strategy, comprising alternating $C_2H_2$ and HCl treatments, to synthesise high-loading (10 wt%) Ru, Ir and Rh catalysts on carbon supports with controlled metal nuclearity in the subnanometre regime. Precise size control (±0.1 nm) is enabled by regulating the number of $C_2H_2$–HCl cycles. The avoidance of NP surface overchlorination, which hinders $C_2H_2$ adsorption, is identified as key for the remarkable efficacy of the $C_2H_2$–HCl alternating strategy, as demonstrated by inhibition of the redispersion process resulting from both the $C_2H_2$–HCl cofeeding and inverse sequence (*i.e.*, HCl first) approaches. Detailed characterisation, including XAS, EPR and time-resolved MS analyses revealed that the metal NP redispersion follows a layer-by-layer process in which $C_2H_2$ promotes the migration of surface $MO_xCl_y/MCl_y$ species to the carbon support while HCl regenerates them *via* chlorination of the newly-formed surface $MO_x/M$ species.

For future endeavours, the $C_2H_2$–HCl alternating redispersion approach offers a compelling synthetic route to finely tune metal nuclearity at high loadings and on practical supports, one of the most challenging aspects in nanoscale engineering of catalytic materials. Such control will be central to (i) derive structure–performance relationships at high density of active sites, where metal site proximity may give rise to enhanced catalytic performance,[42] and (ii) implement the acquired knowledge in the design of supported metal catalysts with defined nuclearity for large-scale, targeted applications. To this end, the modulation of the coordination environment of the redispersed metal species constitutes an additional synthetic parameter that will require dedicated studies for optimal catalytic behaviour. Finally, the scale-up amenability of the presented redispersion protocol holds promise for high throughout synthesis, to ultimately produce commercial supported low-nuclearity metal catalysts.

## Conflicts of interest

There are no conflicts to declare.

## Acknowledgements

This publication was created as part of NCCR Catalysis, a National Centre of Competence in Research funded by the Swiss National Science Foundation. The authors thank the Scientific Center for Optical and Electron Microscopy at the

 

ETH Zürich, ScopeM and the SuperXAS beamline at PSI, for access to their facilities.

## References

1 X. F. Yang, A. Wang, B. Qiao, J. Li, J. Liu and T. Zhang, *Acc. Chem. Res.*, 2013, **46**, 1740.
2 S. Mitchell and J. Pérez-Ramírez, *Nat. Rev. Mater.*, 2021, **6**, 969.
3 L. Liu and A. Corma, *Nat. Rev. Mater.*, 2020, **6**, 244.
4 H. Rong, S. Ji, J. Zhang, D. Wang and Y. Li, *Nat. Commun.*, 2020, **11**, 5884.
5 T. Sun, S. Mitchell, J. Li, P. Lyu, X. Wu, J. Pérez-Ramírez and J. Lu, *Adv. Mater.*, 2021, **33**, e2003075.
6 S. Tian, Q. Fu, W. Chen, Q. Feng, Z. Chen, J. Zhang, W. C. Cheong, R. Yu, L. Gu, J. Dong, J. Luo, C. Chen, Q. Peng, C. Draxl, D. Wang and Y. Li, *Nat. Commun.*, 2018, **9**, 2353.
7 E. Vorobyeva, E. Fako, Z. Chen, S. M. Collins, D. Johnstone, P. A. Midgley, R. Hauert, O. V. Safonova, G. Vilé, N. López, S. Mitchell and J. Pérez-Ramírez, *Angew. Chem.*, 2019, **131**, 8816.
8 D. Faust Akl, A. Ruiz-Ferrando, E. Fako, R. Hauert, O. Safonova, S. Mitchell, N. López and J. Pérez-Ramírez, *ChemCatChem*, 2021, **13**, 3247.
9 X. Han, X. Ling, D. Yu, D. Xie, L. Li, S. Peng, C. Zhong, N. Zhao, Y. Deng and W. Hu, *Adv. Mater.*, 2019, **31**, e1905622.
10 S. Dai, J. P. Chou, K. W. Wang, Y. Y. Hsu, A. Hu, X. Pan and T. Y. Chen, *Nat. Commun.*, 2019, **10**, 440.
11 K. Yamamoto, T. Imaoka, M. Tanabe and T. Kambe, *Chem. Rev.*, 2020, **120**, 1397.
12 M. B. Gawande, P. Fornasiero and R. Zbořil, *ACS Catal.*, 2020, **10**, 2231.
13 Y. Zhou, X. Tao, G. Chen, R. Lu, D. Wang, M. X. Chen, E. Jin, J. Yang, H. W. Liang, Y. Zhao, X. Feng, A. Narita and K. Müllen, *Nat. Commun.*, 2020, **11**, 5892.
14 C. Xia, Y. Qiu, Y. Xia, P. Zhu, G. King, X. Zhang, Z. Wu, J. Y. T. Kim, D. A. Cullen, D. Zheng, P. Li, M. Shakouri, E. Heredia, P. Cui, H. N. Alshareef, Y. Hu and H. Wang, *Nat. Chem.*, 2021, **13**, 887.
15 Q. Wang, X. Huang, Z. L. Zhao, M. Wang, B. Xiang, J. Li, Z. Feng, H. Xu and M. Gu, *J. Am. Chem. Soc.*, 2020, **142**, 7425.
16 J. Wu, L. Xiong, B. Zhao, M. Liu and L. Huang, *Small Methods*, 2019, **4**, 1900540.
17 L. Liu and A. Corma, *Chem. Rev.*, 2018, **118**, 4981.
18 K. Morgan, A. Goguet and C. Hardacre, *ACS Catal.*, 2015, **5**, 3430.
19 S. Feng, X. Song, Y. Liu, X. Lin, L. Yan, S. Liu, W. Dong, X. Yang, Z. Jiang and Y. Ding, *Nat. Commun.*, 2019, **10**, 5281.
20 S. Feng, P. Hemberger, A. Bodi, X. Song, T. Yu, Z. Jiang, Y. Liu and Y. Ding, *J. Catal.*, 2020, **382**, 347.
21 A. Krapp, K. K. Pandey and G. Frenking, *J. Am. Chem. Soc.*, 2007, **129**, 7596.
22 T. Wang, *J. Catal.*, 1981, **70**, 187.
23 S. K. Kaiser, R. Lin, F. Krumeich, O. V. Safonova and J. Pérez-Ramírez, *Angew. Chem., Int. Ed.*, 2019, **58**, 12297.
24 R. Lin, S. K. Kaiser, R. Hauert and J. Pérez-Ramírez, *ACS Catal.*, 2018, **8**, 1114.
25 D. J. Morgan, *Surf. Interface Anal.*, 2015, **47**, 1072.
26 O. Muller, M. Nachtegaal, J. Just, D. Lutzenkirchen-Hecht and R. Frahm, *J. Synchrotron Radiat.*, 2016, **23**, 260.
27 P. M. Abdala, O. V. Safonova, G. Wiker, W. van Beek, H. Emerich, J. A. van Bokhoven, J. Sa, J. Szlachetko and M. Nachtegaal, *Chimia*, 2012, **66**, 699.
28 A. H. Clark, J. Imbao, R. Frahm and M. Nachtegaal, *J. Synchrotron Radiat.*, 2020, **27**, 551.
29 M. Newville, *J. Synchrotron Radiat.*, 2001, **8**, 322.
30 E. Gallegos-Suarez, A. Guerrero-Ruiz, I. Rodriguez-Ramos and A. Arcoya, *Chem. Eng. J.*, 2015, **262**, 326.
31 J. L. Gómez de la Fuente, M. V. Martínez-Huerta, S. Rojas, P. Hernández-Fernández, P. Terreros, J. L. G. Fierro and M. A. Peña, *Appl. Catal., B*, 2009, **88**, 505.
32 S. Stoll and A. Schweiger, *J. Magn. Reson.*, 2006, **178**, 42.
33 J. R. Pilbrow, *Transition Ion Electron Paramagnetic Resonance*, Clarendon Press, Oxford, 1990.
34 Y. Pu, J. Zhang, L. Yu, Y. Jin and W. Li, *Appl. Catal., A*, 2014, **488**, 28.
35 B. Wang, Y. Yue, S. Wang, Z. Chen, L. Yu, S. Shao, G. Lan, Z. Pan, J. Zhao and X. Li, *Chem. Commun.*, 2020, **56**, 10722.
36 X. Duan, X. Tian, J. Ke, Y. Yin, J. Zheng, J. Chen, Z. Cao, Z. Xie and Y. Yuan, *Chem. Sci.*, 2016, **7**, 3181.
37 H. Hillebrecht, P. J. Schmidt, H. W. Rotter, G. Thiele, P. Zönnchen, H. Bengel, H. J. Cantow, S. N. Magonov and M. H. Whangbo, *J. Alloys Compd.*, 1997, **246**, 70.
38 E. Solari, S. Antonijevic, S. Gauthier, R. Scopelliti and K. Severin, *Eur. J. Inorg. Chem.*, 2007, **2007**, 367.
39 P. J. Carl and S. C. Larsen, *J. Catal.*, 2000, **196**, 352.
40 B.-Z. Wan and J. H. Lunsford, *Inorg. Chim. Acta*, 1982, **65**, L29.
41 S. K. Kaiser, I. Surin, A. Amoros-Perez, S. Büchele, F. Krumeich, A. H. Clark, M. C. Román-Martínez, M. A. Lillo-Ródenas and J. Pérez-Ramírez, *Nat. Commun.*, 2021, **12**, 4016.
42 Z. Jin, P. Li, Y. Meng, Z. Fang, D. Xiao and G. Yu, *Nat. Catal.*, 2021, **4**, 615.